

## RESEARCH ARTICLE

View Article Online  
View Journal

Cite this: DOI: 10.1039/d5qi00986c

## Star-shaped Pt(II) complexes with excellent optical power limiting performance and their flexible optical limiters†

Lai Hu, Zhiyuan Chen, Zhi Zhao, Ruiqi Chen, Senqiang Zhu, \* Rui Liu \* and Hongjun Zhu

Efficient optical power limiting (OPL) materials are crucial for protecting optical devices and the eyes. However, achieving strong OPL responses while maintaining high optical transparency and processability remains a challenge. Herein, we report a molecular design strategy to improve the OPL performance of a series of Pt(II) complexes (**Pt-1a–Pt-2c**) by incorporating trinuclear Pt centers and modulating the core-ethynyl ligand electronic interactions. The trinuclear Pt centers extended the triplet-state lifetimes (0.52–2.05  $\mu\text{s}$ ) and enhanced the excited-state absorption (ESA), while the core-ethynyl ligand interactions effectively tuned the ground- and excited-state properties. These complexes exhibited tunable nonlinear optical (NLO) and OPL properties at 532 nm, with a minimum normalized transmittance ( $T_{\text{min}}$ ) in the range of 0.38–0.78. Notably, **Pt-2b** showed outstanding OPL performance with a nonlinear absorption coefficient ( $\beta_{\text{eff}}$ ) and optical limiting threshold ( $F_{\text{OL}}$ ) of 192.15  $\text{cm GW}^{-1}$  and 0.71  $\text{J cm}^{-2}$ , respectively. In flexible films, **Pt-2b@PDMS-1.00 wt%** demonstrated markedly enhanced OPL performance ( $\beta_{\text{eff}} = 965.83 \text{ cm GW}^{-1}$ ,  $F_{\text{OL}} = 0.26 \text{ J cm}^{-2}$ ), surpassing the performance of many reported OPL materials. This study provides valuable insights into designing transparent Pt(II) complexes with superior OPL properties, and highlights the promise of flexible films for photonic applications.

Received 21st April 2025,  
Accepted 26th June 2025

DOI: 10.1039/d5qi00986c

rsc.li/frontiers-inorganic

## Introduction

Nonlinear optical (NLO) materials have garnered significant interest owing to their broad applications in pulsed laser generation, optical power limiting (OPL), optical switching, and bioimaging.<sup>1–4</sup> OPL materials are particularly valuable as they attenuate high-energy laser pulses to protect sensitive optical devices and the human eyes while maintaining high transmittance for low-energy light. Ideal OPL materials should possess rapid response times, low limiting thresholds, high transparency, and good stability. Currently developed OPL materials include inorganic compounds,<sup>5,6</sup> organic  $\pi$ -conjugated molecules,<sup>7,8</sup> organometallic complexes (Pt and Ir systems),<sup>9–12</sup> metal–organic frameworks (MOFs),<sup>13–17</sup> clusters (metal and metal-oxo clusters),<sup>18–22</sup> carbon materials,<sup>23,24</sup> two-dimensional (2D) materials,<sup>25,26</sup> and composites.<sup>27,28</sup> However, many of these materials still suffer from certain limitations. For

instance,  $\text{C}_{60}$  and porphyrins/phthalocyanines show strong OPL activity but suffer from intense absorption in the 400–700 nm visible range, which reduces its transparency. Although, 2D materials offer broadband OPL responses, they often exhibit poor dispersibility, and materials such as black phosphorus also suffer from limited stability. Thus, developing high-performance OPL materials that combine excellent transparency, stability, and processability, along with solid-state OPL limiters that are suitable for diverse applications remains a critical challenge in this field.

Square-planar Pt(II) complexes exhibit intriguing photo-physical properties<sup>29</sup> and have been widely explored in organic light-emitting devices (OLEDs),<sup>30</sup> OPL,<sup>31</sup> organic solar cells,<sup>32</sup> and self-assembled materials.<sup>33</sup> Notably, Pt-induced efficient intersystem crossing (ISC) generates long-lived triplet states with high quantum yields, facilitating two-photon absorption (TPA) and reverse saturable absorption (RSA), making them promising candidates for OPL applications.<sup>34,35</sup> Cyclometalated Pt(II) complexes show remarkable OPL performance because of their strong spin–orbit coupling (SOC) effect. However, their intense metal-to-ligand charge transfer (MLCT) and ligand-to-ligand charge transfer (LLCT) transitions reduce their optical transparency.<sup>29,36</sup> In contrast, alkylphosphine Pt(II) complexes exhibit weaker MLCT absorption,

School of Chemistry and Molecular Engineering, Nanjing Tech University, Nanjing 211816, China. E-mail: zhuseqiang1993@njtech.edu.cn, rui.liu@njtech.edu.cn

† Electronic supplementary information (ESI) available. CCDC: 2288730–2288732 and 2213945. For ESI and crystallographic data in CIF or other electronic format see DOI: <https://doi.org/10.1039/d5qi00986c>

ensuring better transparency, and phosphine ligands ( $\text{PR}_3$ ) improve solubility. In recent years, Schanze and Zhou *et al.* have reported numerous alkylphosphine  $\text{Pt(II)}$  acetylides and  $\text{Pt(II)}$  polyynes with considerable TPA and RSA effects, successfully demonstrating their OPL applications.<sup>37–41</sup> Some of these molecular systems even outperform  $\text{C}_{60}$  and metalloporphyrins. However, current studies remain focused on linear structures. The weak  $\text{Pt } d_{\pi}-\pi$  orbital mixing limits their OPL activity. Thus, achieving strong OPL responses while maintaining high transparency remains a critical challenge that urgently needs to be addressed in this field.

Star-shaped  $\text{Pt(II)}$  structures are promising candidates to enhance the OPL performance of alkylphosphine  $\text{Pt(II)}$  complexes, with several advantages, such as (1) synergistic interactions among the branches improve the nonlinear polarizability ( $\chi$ );<sup>42,43</sup> (2) trinuclear  $\text{Pt}$  centers introduce strong SOC effects, promoting ISC and enhancing excited-state absorption (ESA);<sup>44</sup> and (3) compared with  $\text{Pt(II)}$ -based dendrimers, star-shaped  $\text{Pt(II)}$  complexes are more synthetically accessible and cost-effective.<sup>45</sup> For example, Zhou *et al.* reported that in V-shaped and star-shaped  $\text{Pt(II)}$  acetylide systems, high-density  $\text{Pt}$  centers efficiently enhanced the SOC effect, improving the OPL activity.<sup>46</sup> Some  $\text{Pt(II)}$  acetylides even surpassed  $\text{C}_{60}$  in OPL performance while maintaining high transparency. Despite their wide use in OLEDs,<sup>44</sup> ion capture,<sup>47</sup> and cancer therapy,<sup>48</sup> star-shaped  $\text{Pt(II)}$  complexes remain underexplored for OPL applications.

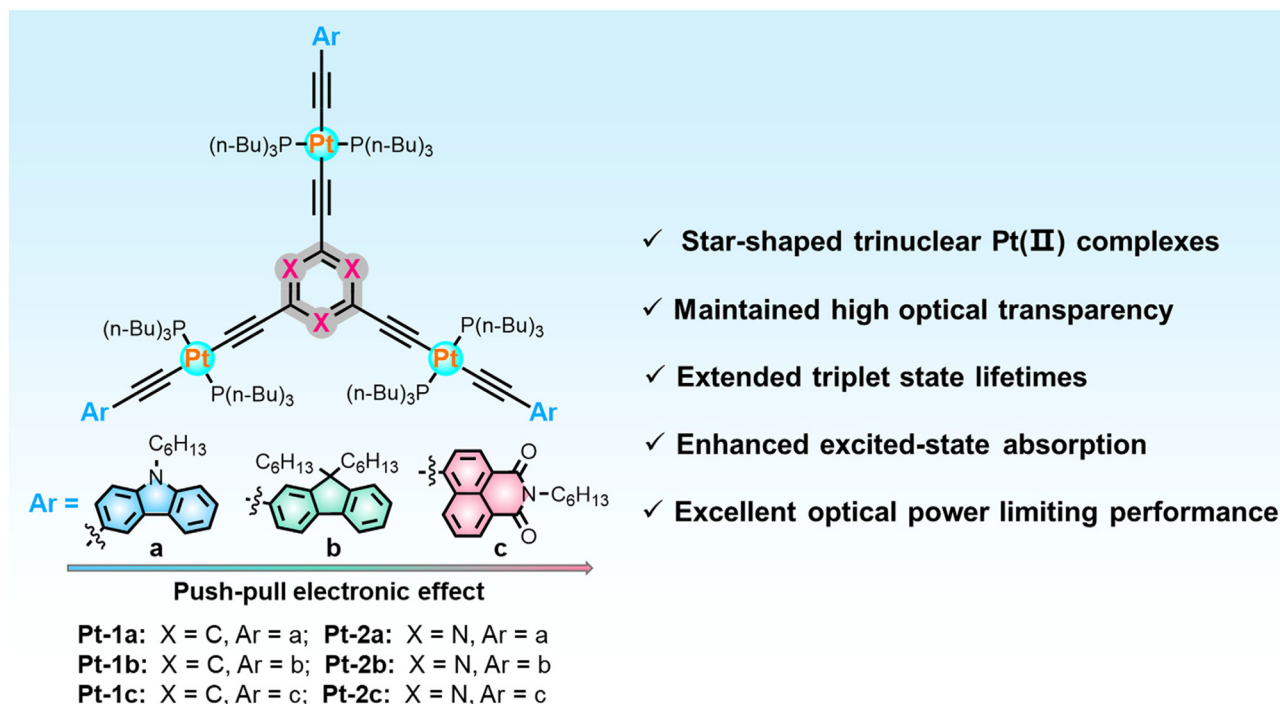
Based on these considerations, we designed a series of star-shaped trinuclear  $\text{Pt(II)}$  complexes (**Pt-1a–Pt-2c**) featuring phenyl and triazine cores to enhance the OPL performance of alkylphosphine  $\text{Pt(II)}$  complexes (Scheme 1). 1,3,5-Triazine, a

strong electron acceptor (ionization potential of 11.67 eV) with an excellent photothermal stability, is widely used in star-shaped  $\pi$ -conjugated systems.<sup>42,49</sup> The incorporation of trinuclear  $\text{Pt}$  centers markedly enhances the ESA. By modulating the electronic interactions between the cores and the ethynyl ligands (carbazole, fluorene, and naphthalimide), the ground- and excited-state properties of **Pt-1a–Pt-2c** were precisely tuned. Additionally, bulky alkyl chains suppressed the aggregation and improved the solubility of these complexes. As expected, **Pt-1a–Pt-2c** exhibited extended triplet state lifetimes and enhanced ESA, with their optical transparency and OPL performance optimized by core-ethynyl ligand interactions. In particular, **Pt-2b** showed the strongest OPL responses at 532 nm while maintaining high transparency. Moreover, the flexible **Pt-2b@PDMS** films displayed remarkable OPL performance, making them ideal candidates for practical OPL applications. This study reveals the essential roles of metal centers and ligand engineering in tuning the OPL properties of  $\text{Pt(II)}$  complexes and provides a new strategy for designing advanced OPL materials.

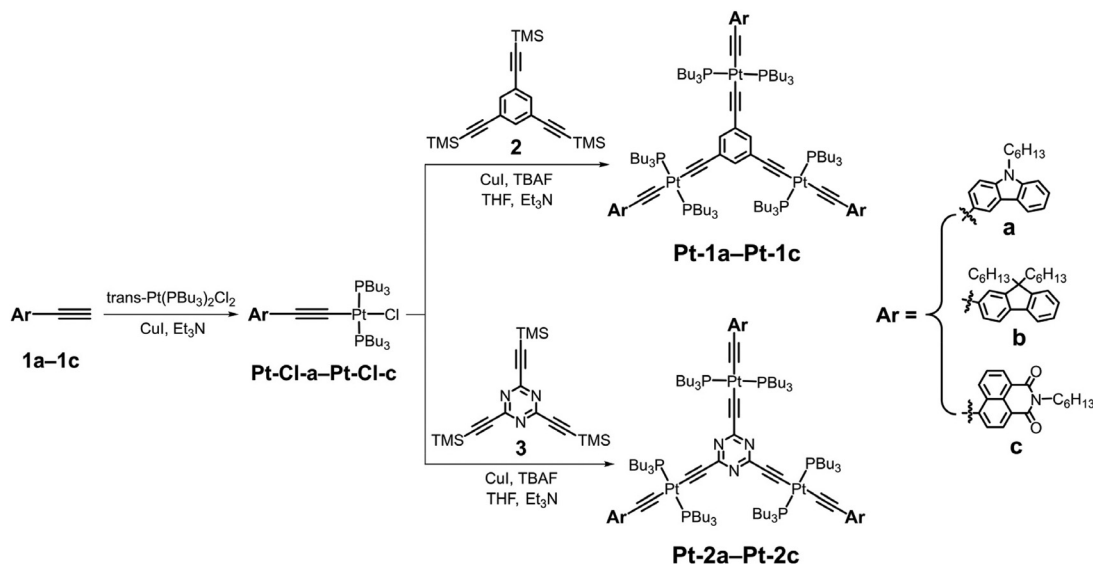
## Results and discussion

### Synthesis and characterization

The synthetic routes for **Pt-1a–Pt-2c** are shown in Scheme 2, with detailed experimental procedures provided in the ESI.† Briefly, compounds **1a–1c** were reacted with *trans*-[Pt( $\text{PBu}_3$ )<sub>2</sub>Cl<sub>2</sub>] via the Sonogashira cross-coupling reactions to afford precursors **Pt-Cl-a–Pt-Cl-c**. In the presence of TBAF, Et<sub>3</sub>N



**Scheme 1** Molecular structures of star-shaped  $\text{Pt(II)}$  complexes **Pt-1a–Pt-2c**.



**Scheme 2** Synthetic routes for **Pt-1a–Pt-2c**.

and CuI, the trimethylsilyl (TMS)-protected compounds **2** or **3** underwent deprotection, followed by *in situ* base-catalyzed dehydrohalogenation reactions with **Pt-Cl-a–Pt-Cl-c** to give **Pt-1a–Pt-2c** in high yields (73%–85%).

**Pt-1a–Pt-2c** were characterized using  $^1\text{H}$ ,  $^{13}\text{C}$ , and  $^{31}\text{P}$  NMR spectroscopies and MALDI-TOF-MS (see ESI $^\dagger$ ). In the  $^{31}\text{P}$  NMR spectra, all complexes displayed sharp singlet signals flanked by two  $^{195}\text{Pt}$  satellites, with  $^1J_{\text{Pt-P}}$  of  $\sim 2350$  Hz, indicating a *trans*-P–Pt–P configuration. These data confirmed the successful synthesis of **Pt-1a–Pt-2c**. They were highly soluble in common organic solvents (*e.g.*, toluene and THF) and exhibited excellent stability (Fig. S25 $^\dagger$ ), with no sensitivity to light or oxygen. TGA curves indicated that the decomposition temperatures ( $T_d$ ) exceeded  $306^\circ\text{C}$ , demonstrating their high thermal stability (Fig. S26 $^\dagger$ ).

### X-Ray crystal structures

The molecular structures of Pt(II) complexes were determined by single-crystal X-ray diffraction. Single crystals of **Pt-1b**, **Pt-2b**, **Pt-1c**, and **Pt-2c** were grown by layering ethanol onto a concentrated  $\text{CH}_2\text{Cl}_2$  solution. Despite multiple attempts, suitable crystals for **Pt-1a** and **Pt-2a** could not be obtained. The crystallographic data are summarized in Tables S1 and S2, $^\dagger$  with selected bond lengths and bond angles listed in Tables S3–S6. $^\dagger$  ORTEP diagrams and packing models are shown in Fig. S27–S30. $^\dagger$

All four complexes crystallized in the triclinic  $P\bar{1}$  space group. The asymmetric units of **Pt-1b**, **Pt-2b**, and **Pt-1c** each contain one molecule, while that of **Pt-2c** contains two. Fig. 1a–d illustrate that the Pt(II) complexes exhibit the anticipated star-shaped structure with each Pt center adopting a slightly distorted square-planar geometry, where the two  $\text{PBu}_3$  groups and ethynyl ligands are in a *trans*-arrangement. The C–Pt–P bond angles range from  $85.2(3)^\circ$  to  $95.7(4)^\circ$ , which allevi-

ates steric hindrance between the  $\text{PBu}_3$  groups. The Pt–P and Pt–C bond lengths ( $2.25(4)$ – $2.41(7)$  Å and  $1.77(12)$ – $2.07(11)$  Å, respectively) are consistent with those of reported alkylphosphine Pt(II) complexes. $^{35,41,50}$

Significant differences are observed in dihedral angles between the cores and ethynyl ligands among the Pt(II) complexes. The dihedral angles between the fluorene units and the core are  $22.43^\circ$ ,  $24.84^\circ$ , and  $80.78^\circ$  for **Pt-1b**, and  $8.41^\circ$ ,  $27.02^\circ$ , and  $58.75^\circ$  for **Pt-2b**. In contrast, **Pt-1c** and **Pt-2c** exhibit obviously smaller dihedral angles between the naphthalimide units and the core, suggesting better coplanarity. In the crystal structures, **Pt-1b** and **Pt-2b** are primarily stabilized by C–H $\cdots\pi$  interactions ( $2.92$ – $3.72$  Å, Fig. 1e and f). Notably, C–H $\cdots\text{Pt}$  interactions ( $2.75$  Å) are also observed in the **Pt-2b** dimer. For the trimers of **Pt-1c** and **Pt-2c**, multiple weak interactions are present, including C–H $\cdots\pi$  ( $2.67$ – $3.61$  Å), C–H $\cdots\text{N}$  ( $3.09$  and  $2.62$  Å), and C–H $\cdots\text{O}$  interactions ( $2.72$  and  $2.57$  Å), as shown in Fig. 1g and h. A summary of these interactions is provided in Table S7. $^\dagger$  The  $\text{PBu}_3$  groups extend the intermolecular contact distances, resulting in the absence of Pt $\cdots$ Pt interactions. Nevertheless, sliding  $\pi$ – $\pi$  stacking are observed between the naphthalimide units in **Pt-1c** and **Pt-2c**, with centroid-to-centroid distances of  $3.53$  and  $3.61$  Å, respectively. These results suggest that the fluorene units in **Pt-1b** and **Pt-2b** introduce significant distortion, effectively suppressing  $\pi$ – $\pi$  stacking and promoting homogeneous dispersion within polymer matrices.

### Photophysical properties

**Absorption spectra.** The UV–vis absorption spectra of **Pt-1a–Pt-2c** were recorded in  $\text{CH}_2\text{Cl}_2$ , with the photophysical parameters summarized in Table 1. As illustrated in Fig. 2a, all the complexes showed intense absorption bands, attributed to Pt center-disturbed  $1\pi$ – $\pi^*$  transitions of ethynyl ligands. **Pt-1a** and

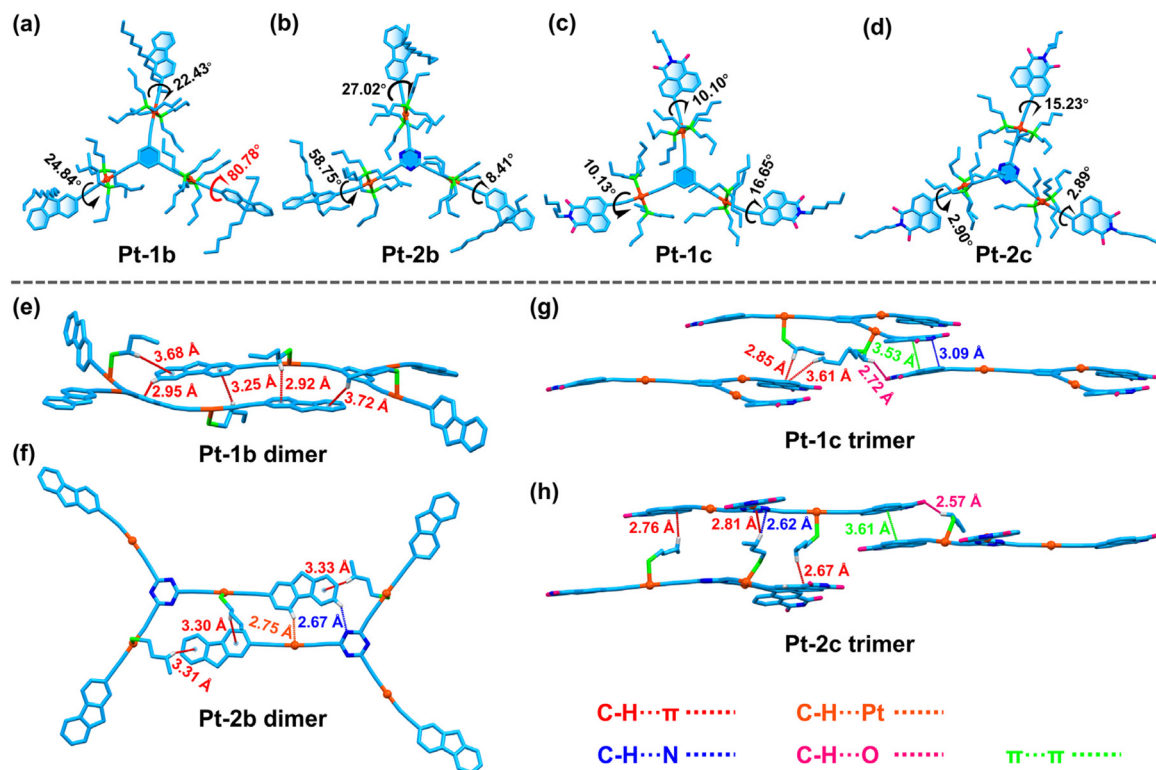


**Fig. 1** (a–d) Single-crystal structures of Pt-1b, Pt-2b, Pt-1c, and Pt-2c (Color codes: cyan-green = C, light gray = H, blue = N, pink = O, green = P, and orange = Pt). (e–h) Crystal packing modes of Pt-1b, Pt-2b, Pt-1c, and Pt-2c. Partial H atoms, C<sub>6</sub>H<sub>13</sub> chains, and PBu<sub>3</sub> groups are omitted for clarity.

**Table 1** Photophysical parameters for Pt-1a–Pt-2c

Complexes	$\lambda_{\text{abs}}^a/\text{nm}$	$\lambda_{\text{em}}/\text{nm}$ ( $\tau_{\text{em}}/\mu\text{s}$ ) <sup>b</sup>	$\lambda_{\text{em}}/\text{nm}$ ( $\tau_{\text{em}}/\mu\text{s}$ ) <sup>c</sup>	$\Phi_P^d/\%$	$\lambda_{T1-Tn}/\text{nm}$ ( $\tau_T/\mu\text{s}$ ) <sup>e</sup>	$\lambda_{\text{cut-off}}/\text{nm}$
Pt-1a	293, 310, 345	401, 462	460 (78.61)	—	—	388
Pt-2a	95, 309, 324, 356	401, 452	453 (37.59)	—	—	405
Pt-1b	297, 358	380, 507 (0.93)	507 (202.04)	15.31	560 (0.96)	383
Pt-2b	299, 352	389, 506 (0.50)	505 (211.40)	18.28	530 (0.52)	395
Pt-1c	284, 320, 349, 435	512, 639 (1.98)	483, 634 (368.01)	6.77	628 (2.05)	498
Pt-2c	298, 427	491	463, 629 (435.75)	—	640 (1.59)	480

<sup>a</sup> UV-vis absorption band maxima in CH<sub>2</sub>Cl<sub>2</sub>. <sup>b</sup> Emission band maxima and phosphorescence lifetimes measured in deaerated CH<sub>2</sub>Cl<sub>2</sub>. <sup>c</sup> Emission band maxima and decay lifetimes of T<sub>1</sub> state recorded in 2-Me THF at 77 K. <sup>d</sup> Absolute phosphorescence quantum yields measured in deaerated CH<sub>2</sub>Cl<sub>2</sub> using an integrating sphere. <sup>e</sup> ns-TA band maxima or triplet state lifetimes in deaerated toluene.

**Pt-2a** displayed two main absorption peaks between 280–390 nm, along with a moderate band at *ca.* 310 nm, likely from metal-centered (MC) transitions.<sup>51</sup> **Pt-1b** and **Pt-2b** exhibited similar absorption features below 400 nm (280–305 nm and 305–380 nm), with maximum absorption wavelengths ( $\lambda_{\text{abs}}$ ) of 358 nm and 352 nm, respectively. However, the cut-off wavelength ( $\lambda_{\text{cut-off}}$ ) of **Pt-2b** was red-shifted by 12 nm. Meanwhile, the d $\pi$ – $\pi$  orbital mixing led to red-shifted absorption compared with their precursors **Pt-Cl-a**–**Pt-Cl-c** (Fig. S31†). Nevertheless, the  $\lambda_{\text{cut-off}}$  of **Pt-1a**, **Pt-2a**, **Pt-1b**, and **Pt-2b** remained below 405 nm, ensuring high optical transparency.

In contrast, **Pt-1c** and **Pt-2c**, bearing naphthalimide units with strong  $^1\pi$ – $\pi^*$  transition absorptions near 430 nm, exhibi-

ted a  $\lambda_{\text{cut-off}}$  extending beyond 480 nm, resulting in reduced transparency. Furthermore, the absorption spectra in different solvents revealed that the absorption peaks of **Pt-2a**, **Pt-2b**, and **Pt-1c** broadened more noticeably in polar solvents (Fig. S32†), indicating stronger intramolecular charge transfer (ICT) effects than **Pt-1a**, **Pt-1b**, and **Pt-2c**. These enhanced ICT characteristics are expected to improve their OPL responses.

**Emission spectra.** The emission spectra of **Pt-1a**–**Pt-2c** in deaerated CH<sub>2</sub>Cl<sub>2</sub> are shown in Fig. 2b. Except for **Pt-2c**, all the complexes exhibited dual emission properties at room temperature. The short-wavelength bands with lifetimes <2 ns were assigned to the lowest singlet state (S<sub>1</sub>) fluorescence.<sup>52</sup> The long-wavelength band, featuring well-resolved vibrational



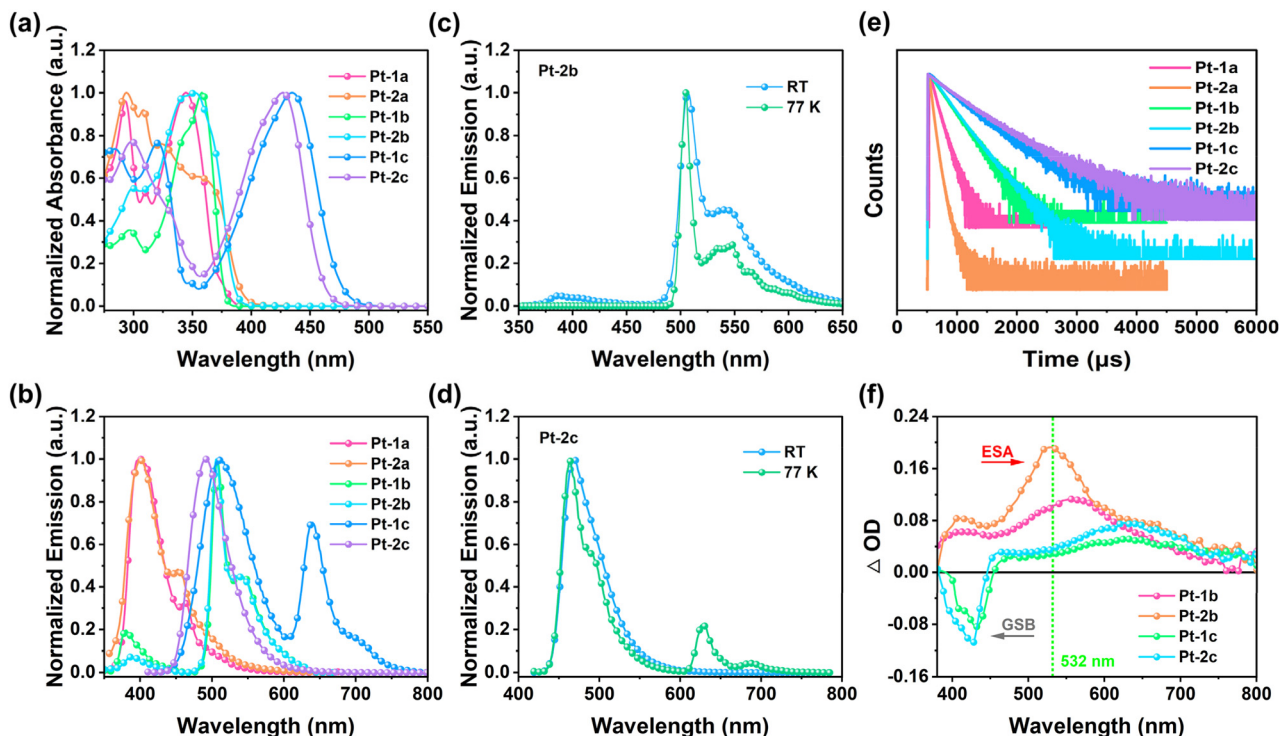


**Fig. 2** (a) UV-vis absorption spectra of **Pt-1a**–**Pt-2c** in  $\text{CH}_2\text{Cl}_2$  and (b) emission spectra of **Pt-1a**–**Pt-2c** in deaerated  $\text{CH}_2\text{Cl}_2$  ( $c = 1.0 \times 10^{-5} \text{ mol L}^{-1}$ , r.t.). (c and d) Normalized emission spectra of **Pt-2b** and **Pt-2c** in 2-Me THF at r.t. and 77 K, respectively. (e) Emission lifetimes of the  $T_1$  state for **Pt-1a**–**Pt-2c** at 77 K. (f) ns-TA spectra of **Pt-1b**, **Pt-2b**, **Pt-1c**, and **Pt-2c** at zero delay in deaerated toluene ( $\lambda_{\text{ex}} = 355 \text{ nm}$ ).

structures, microsecond-scale lifetimes and large Stokes shifts ( $>100 \text{ nm}$ ), corresponded to the lowest triplet state ( $T_1$ ) phosphorescence.

The ethynyl ligands successfully influenced the emission properties. For **Pt-1a** and **Pt-2a**, phosphorescence appeared as weak shoulders beside fluorescence, while for **Pt-1b** and **Pt-2b** phosphorescence was the predominant emission. **Pt-2c** showed only cyan fluorescence with  $\lambda_{\text{em}} = 491 \text{ nm}$ , which was blue-shifted by 20 nm compared with **Pt-1c**, with a higher fluorescence quantum yield ( $\Phi_{\text{F}} = 5.40\%$ ) than the others ( $\Phi_{\text{F}} < 0.05\%$ ). The low  $\Phi_{\text{F}}$  values were attributed to the heavy-atom effect of Pt centers, which enhanced the SOC effect and facilitated ISC from the  $S_1$  state to  $T_1$  state. The absolute phosphorescence quantum yields ( $\Phi_{\text{P}}$ ) for **Pt-1b**, **Pt-2b**, and **Pt-1c** were 15.31%, 18.28%, and 6.77%, respectively (Table 1). Notably, the incorporation of fluorene units enhanced the  $d_{\pi-\pi}$  orbital coupling, increasing the  $T_1$  state populations. **Pt-2b** showed the highest  $\Phi_{\text{P}}$ , which could improve the OPL performance *via* the RSA mechanism.

The fluorescence peaks of **Pt-1a**–**Pt-2c** exhibited red-shifts with increasing solvent polarity, suggesting that the  $S_1$  state originated from the mixed  $^1\pi-\pi^*/^1\text{ICT}$  transitions. In contrast, the phosphorescence bands, which were attributed to the predominant  $^3\pi-\pi^*$  transitions, were almost unaffected by solvent polarity (Fig. S33<sup>†</sup>). These assignments were also supported by theoretical calculations. To further explore the  $T_1$  emissive state properties, low-temperature emission spectra were

recorded (Fig. 2c, d, and S34<sup>†</sup>). At 77 K, the long-wavelength bands intensified, and their lifetimes were greatly extended (Fig. 2e and Table 1), confirming their phosphorescent origin. However, **Pt-1c** and **Pt-2c** still displayed intense fluorescence, suggesting lower  $T_1$  state populations despite their long phosphorescence lifetimes.<sup>41,46</sup>

**Nanosecond transient absorption spectra.** The triplet state properties of **Pt-1a**–**Pt-2c** were investigated using ns-TA spectroscopy. Except for the weak TA signals of **Pt-1a** and **Pt-2a**, the TA spectra at zero delay and time-resolved TA profiles of the Pt (II) complexes in deaerated toluene are presented in Fig. 2f and Fig. S35<sup>†</sup>. These complexes exhibited broad and intense ESA bands in the visible to NIR region (380–800 nm for **Pt-1b** and **Pt-2b** and 450–800 nm for **Pt-1c** and **Pt-2c**), which were stronger than their GSA, indicating the potential for RSA effects. **Pt-1c** and **Pt-2c** displayed distinct bleaching bands in the range of 380–450 nm, which were consistent with the GSA (Fig. 2a), confirming that their excited-states are localized on the naphthalimide units. Therefore, the observed triplet states predominantly originated from the ligand-centered  $^3\pi-\pi^*$  transitions.<sup>53</sup>

Fitting the decay curves of the TA signals yielded the triplet state lifetimes ( $\tau_{\text{T}}$ ) for **Pt-1b**, **Pt-2b**, **Pt-1c**, and **Pt-2c** as 0.96, 0.52, 2.05, and 1.59  $\mu\text{s}$ , respectively (Fig. S36<sup>†</sup>), indicating their characteristic as long-lived RSA materials. Compared with the precursors (**Pt-Cl-b** and **Pt-Cl-c**), they showed significantly enhanced ESA signals and 3–6 times longer triplet lifetimes

(Fig. S37<sup>†</sup>), highlighting the great potential of star-shaped Pt (II) complexes in optimizing the triplet state properties. Although incorporation of the triazine core slightly shortened the triplet state lifetimes of **Pt-2b** and **Pt-2c**, it improved their ESA intensity, facilitating the RSA effect. Specifically, **Pt-2b** showed the strongest ESA across the entire TA spectra, indicating its superior triplet state characteristics and promising OPL responses.

### Theoretical calculations

**Molecular orbital analysis.** To understand the observed photophysical phenomena, DFT and TD-DFT calculations were performed to analyze the frontier molecular orbitals (FMOs) of **Pt-1a–Pt-2c** (Fig. 3a and S38–S43<sup>†</sup>). The contributions of each fragment to the FMOs are listed in Tables S8–S13,<sup>†</sup> and the excited-state parameters for the  $S_1$  and  $T_1$  states are summarized in Table 2. As illustrated in Fig. 3a, after introducing triazine core, the LUMO (L) levels of **Pt-2a** and **Pt-2b** are greatly reduced compared with **Pt-1a** and **Pt-1b**, with the energy gaps ( $E_g$ ) decreasing by 0.47 and 0.35 eV, respectively. In contrast, the triazine of **Pt-2c**, lowers the HOMO(H) level by 0.20 eV relative to **Pt-1c**, increasing  $E_g$  to 3.35 eV and resulting in a 40 nm blue-shift in  $\lambda_{abs}$ .

Upon photoexcitation, **Pt-1a–Pt-2c** exhibit intraligand  $^1\pi-\pi^*$  transitions, accompanied by varying degrees of  $^1\text{ICT}$  effects. Specifically, the H and H–1 of **Pt-1a** and **Pt-1b** were delocalized

over the entire molecule, while the L and L+1 were mainly localized on the carbazole or fluorene units, exhibiting predominantly  $^1\pi-\pi^*$  transitions with minor  $^1\text{MLCT}/^1\text{LLCT}$  features. In **Pt-2a**, **Pt-2b**, and **Pt-1c**, the H and H–1 were mainly localized on the carbazole, fluorene, or phenyl, while the L and L+1 were distributed on the triazine core or naphthalimide units, indicating pronounced  $^1\text{LLCT}$  transitions (e.g., carbazole or fluorene  $\rightarrow$  triazine, phenyl  $\rightarrow$  naphthalimide). For **Pt-2c**, the electron density was entirely localized on the naphthalimide units, exhibiting predominately  $^1\pi-\pi^*$  transitions. Additionally, the Pt atoms contribute differently to their FMOs. For **Pt-1a**, **Pt-1c**, and **Pt-2c**, the Pt atoms contribute 10.50–25.80% to the H and H–1, while their contribution to the L and L+1 is negligible, suggesting some  $^1\text{MLCT}$  (Pt  $\rightarrow$  ethynyl ligands) features. In contrast, Pt atoms contribute more ( $>3.07\%$ ) to the L and L+1 of **Pt-1b** and **Pt-2b**, imparting slight ligand-to-metal charge transfer ( $^1\text{LMCT}$ ) transitions, which are beneficial for enhancing their OPL responses.<sup>41</sup>

**Natural transition orbital analysis.** To investigate the origin of phosphorescent emission in **Pt-1a–Pt-2c**,<sup>45</sup> natural transition orbitals (NTOs) were calculated based on the optimized  $T_1$  state geometries. As presented in Fig. 3b, the hole  $\rightarrow$  particle transitions contributed over 97.2% to the  $T_1$  state. The ethynyl ligands accounted for more than 82.17% to both hole and particle, while the contribution from Pt atoms ranged from 2.29% to 11.14%, with a higher contribution to the hole

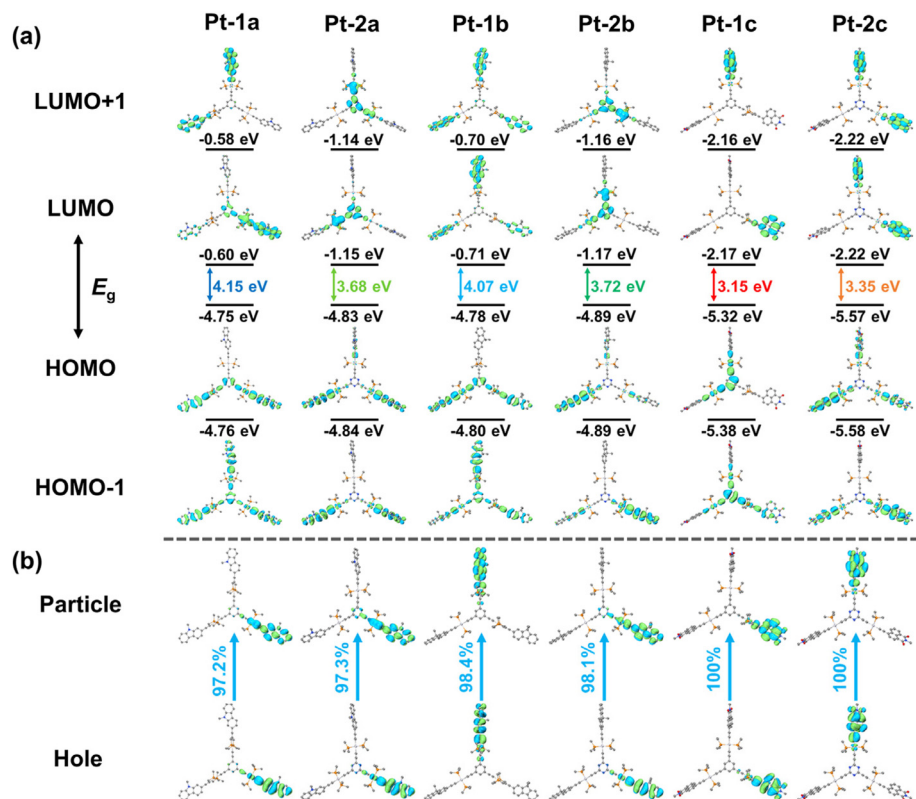


**Fig. 3** (a) Contour plots of HOMO, HOMO–1, LUMO, and LUMO+1 for **Pt-1a–Pt-2c** based on optimized  $S_0$  geometries. (b) Distribution patterns of NTOs for  $S_0 \rightarrow T_1$  excitation of **Pt-1a–Pt-2c** based on optimized  $T_1$  geometries.

**Table 2** Excitation energies (eV), wavelengths (nm), oscillator strengths (*f*), and dominant contributing configurations of the  $S_1$  and  $T_1$  states for **Pt-1a–Pt-2c** based on their optimized  $S_0$  geometries

Complexes	State	Excitation energy/eV (Wavelength/nm)	<i>f</i>	Orbital contribution (>10%)	Assignment
<b>Pt-1a</b>	$S_1$	3.60 (344)	0.440	H → L (38%), H → L+3 (11%)	$^1\text{IL}/^1\text{MLCT}$
	$T_1$	2.67 (463)	0.000	H-3 → L+3 (15%), H-4 → L+4 (13%)	$^3\text{IL}/^3\text{MLCT}/^3\text{LLCT}$
<b>Pt-2a</b>	$S_1$	3.23 (383)	0.088	H → L (68%), H-2 → L (17%)	$^1\text{IL}/^1\text{LLCT}$
	$T_1$	2.69 (460)	0.000	H → L+2 (57%)	$^3\text{IL}/^3\text{MLCT}$
<b>Pt-1b</b>	$S_1$	3.58 (346)	0.963	H → L+2(18%), H → L+3 (25%)	$^1\text{IL}/^1\text{LLCT}/^1\text{LMCT}$
	$T_1$	2.60 (476)	0.000	H-1 → L (62%)	$^3\text{IL}/^3\text{LLCT}$
<b>Pt-2b</b>	$S_1$	3.26 (380)	0.0366	H → L (81%)	$^1\text{IL}/^1\text{LLCT}/^1\text{LMCT}$
	$T_1$	2.61 (475)	0.000	H → L+2 (62%)	$^3\text{IL}/^3\text{MLCT}$
<b>Pt-1c</b>	$S_1$	2.77 (447)	0.001	H → L (68%), H-1 → L (19%)	$^1\text{IL}/^1\text{MLCT}/^1\text{LLCT}$
	$T_1$	1.97 (629)	0.000	H-4 → L (57%), H-1 → L (21%)	$^3\text{IL}/^3\text{MLCT}/^3\text{LLCT}$
<b>Pt-2c</b>	$S_1$	3.04 (407)	1.138	H → L (67%)	$^1\text{IL}/^1\text{MLCT}$
	$T_1$	1.98 (626)	0.000	H → L (82%)	$^3\text{IL}/^3\text{MLCT}$

(Table S14†). These results indicated that the  $T_1$  state of **Pt-1a–Pt-2c** primarily originated from  $^3\pi\text{-}\pi^*$  transitions, with a minor  $^3\text{MLCT}$  character, consistent with the experimental observations. The contribution of Pt atoms to both the hole and particle in **Pt-1c** and **Pt-2c** was lower than the other complexes, indicating a weaker  $d_{\pi}\text{-}\pi$  coupling and consequently inhibiting the ISC process. The intense fluorescence observed for **Pt-1c** and **Pt-2c** at 77 K further supported this conclusion.

### Nonlinear optical properties

**Third-order nonlinear optical properties.** Based on the broad and intense ESA signals observed in the ns-TA spectra, the NLO properties were evaluated using an open-aperture Z-scan technique (Fig. 4a). Detailed experimental procedures and data fitting for the Z-scan are included in the ESI.† Under 532 nm pulsed laser irradiation (4.0 ns, 100  $\mu\text{J}$ ), the Z-scan curves of **Pt-1a–Pt-2c** in toluene exhibited obvious RSA characteristics (Fig. 4b and S44†), with the minimum normalized transmittance ( $T_{\min}$ ) at the focal point ( $Z = 0$ ) ranging from 0.38 to 0.78, indicating tunable NLO properties. As expected, **Pt-2b** showed the lowest  $T_{\min}$  value of 0.38, demonstrating the best NLO properties.

To quantitatively compare their NLO properties, the effective nonlinear absorption coefficients ( $\beta_{\text{eff}}$ ) were extracted by fitting the Z-scan data. **Pt-2a** (31.60  $\text{cm GW}^{-1}$ ), **Pt-2b** (192.15  $\text{cm GW}^{-1}$ ), and **Pt-1c** (83.52  $\text{cm GW}^{-1}$ ) showed higher  $\beta_{\text{eff}}$  values than **Pt-1a** (26.49  $\text{cm GW}^{-1}$ ), **Pt-1b** (125.33  $\text{cm GW}^{-1}$ ), and **Pt-2c** (67.45  $\text{cm GW}^{-1}$ ), which can be attributed to their stronger ICT effects (Fig. 4c). The  $\beta_{\text{eff}}$  value of **Pt-2b** surpassed those of most alkylphosphine Pt(II) complexes,<sup>29,54,55</sup> many cyclometalated Pt(II) complexes<sup>9,28</sup> and Pt(II)-incorporated copolymers.<sup>56</sup> The outstanding NLO response of **Pt-2b** originated from the strong SOC-facilitated ISC, along with ICT effects, which synergistically enhanced its ESA.

**Optical power limiting performance.** OPL is a key application in the NLO field. At low incident fluence, **Pt-1a–Pt-2c** showed a linear input–output relationship with high transmittance. As fluence increased, the output fluence gradually decreased and tended to saturate, displaying a typical OPL behavior (Fig. 4d). The OPL performance followed the trend of

**Pt-2b > Pt-1b > Pt-1c > Pt-2c > Pt-2a > Pt-1a**, which was consistent with the Z-scan results. Compared with electron-donating carbazole and electron-withdrawing naphthalimide units, the weakly donating fluorene units in **Pt-1b** and **Pt-2b** enhanced their OPL performance. As shown in Fig. 4e, the optical limiting thresholds ( $F_{\text{OL}}$ , defined as the incident fluence at 50% linear transmittance) for **Pt-1b** and **Pt-2b** were 0.88 and 0.71  $\text{J cm}^{-2}$ , respectively. Owing to the strong ESA, they exhibited markedly enhanced NLO and OPL performances compared with their precursor **Pt-Cl-b** (Fig. 4f and g).

The OPL mechanism is illustrated in the Jablonski diagram (Fig. 4h). Under 532 nm excitation, the molecule underwent rapid ISC from the  $S_1$  state to the  $T_1$  state. The long triplet state lifetimes enabled the accumulation of  $T_1$  state populations and promoted the subsequent  $T_1\text{-}T_n$  absorption (ESA), thereby inducing OPL effects. Therefore, the OPL performance of **Pt-1a–Pt-2c** closely correlated with their ESA intensity. **Pt-2b** exhibited the strongest ESA at 532 nm, thus achieving the best OPL performance. Although **Pt-1c** and **Pt-2c** showed lower  $T_1$  state populations, their long triplet state lifetimes (1.59 and 2.05  $\mu\text{s}$ ) and moderate ESA intensities still provided considerable OPL responses. In contrast, the undetectable ESA signals of **Pt-1a** and **Pt-2a** in the TA spectra accounted for their weak OPL activities.

### Solid-state optical limiter

Solid-state optical limiters offer many advantages for practical applications. Various OPL materials have been successfully integrated into polymer matrices, such as poly(methyl methacrylate) (PMMA), methyltriethoxysilane (MTES), and PDMS, to fabricate doped films or gel glasses.<sup>57–60</sup> Given the high transparency and superior OPL performance of **Pt-2b**, it was incorporated into PDMS to fabricate flexible and transparent **Pt-2b@PDMS** films (Fig. 5a). As a chemically inert material with excellent optical transparency, thermal stability, and flexibility, PDMS ensured uniform dispersion of **Pt-2b** without any chemical interactions.<sup>14,59</sup> **Pt-2b@PDMS** films with various concentrations (0–1.00 wt%) displayed uniform color and smooth, defect-free surfaces that are suitable for optical measurements (Fig. 5b). SEM-EDS analysis confirmed the homogeneous dis-

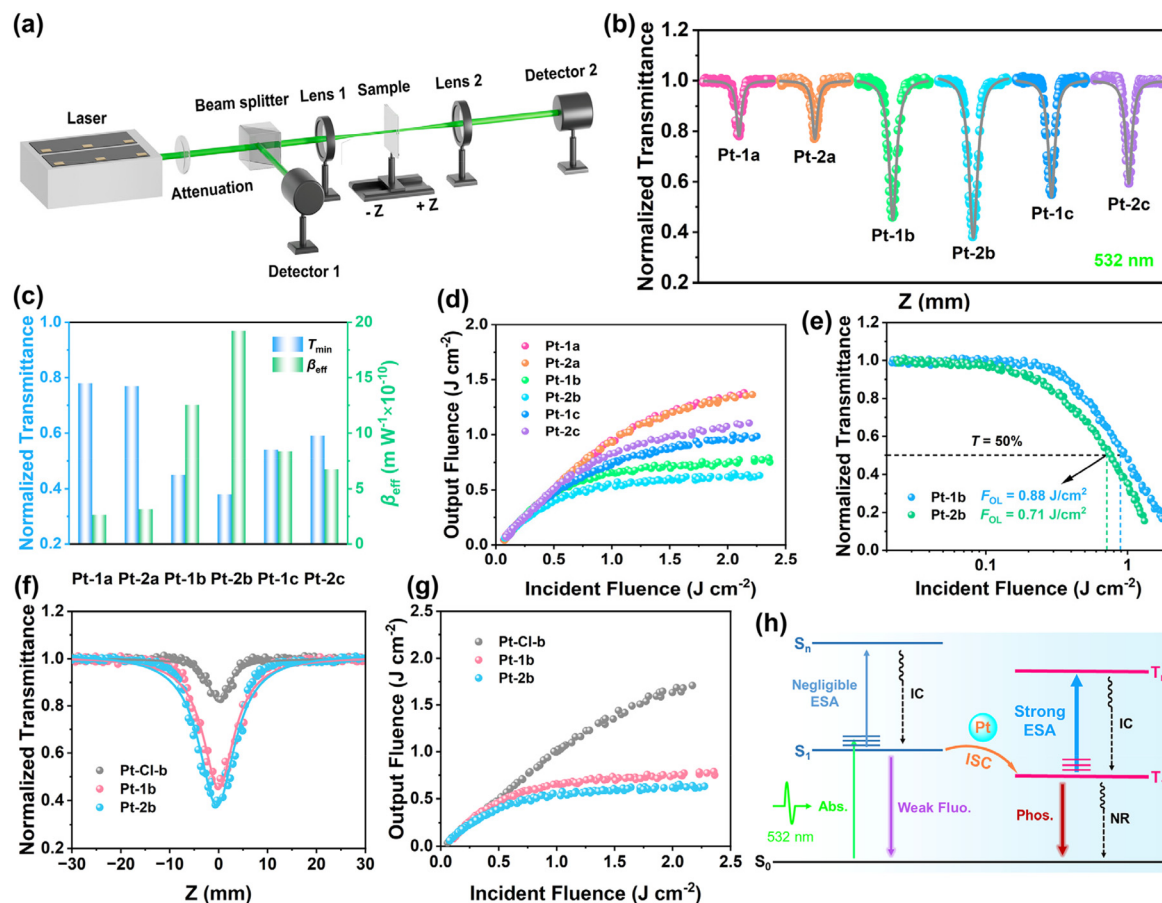


**Fig. 4** (a) Schematic of the Z-scan setup. (b) Open-aperture Z-scan (points) and theoretical fit (solid lines) curves of **Pt-1a–Pt-2c** in toluene ( $c = 1.0 \text{ mM}$ ) at 532 nm. (c) Comparison of the  $T_{\min}$  and  $\beta_{\text{eff}}$  value for **Pt-1a–Pt-2c**. (d) Output fluence versus input fluence curves for **Pt-1a–Pt-2c**. (e) Nonlinear transmittance versus input fluence curves of **Pt-1b** and **Pt-2b**. (f) Open-aperture Z-scan curves and (g) output fluence versus input fluence curves for **Pt-Cl-b**, **Pt-1b**, and **Pt-2b**. (h) Jablonski diagram for **Pt-1a–Pt-2c** based on the RSA mechanism.

tribution of **Pt-2b** within the PDMS matrix (Fig. S45†). Under visible light, the films maintained high optical transparency, clearly revealing the underlying patterns. The pristine PDMS film displayed a linear transmittance ( $T_0$ ) above 90% across the visible spectrum. With increasing **Pt-2b** content,  $T_0$  gradually decreased; for **Pt-2b@PDMS-1.00 wt%**, the  $T_0$  value at 532 nm remained 67%, meeting the practical OPL requirements (Fig. 5c). Even at an increased concentration of 5.00 wt%, **Pt-2b** remained uniformly dispersed in the PDMS matrix (Fig. S46†) owing to its twisted molecular structure and lack of  $\pi$ - $\pi$  stacking, which effectively prevented aggregation, along with bulky alkyl chains that enhanced its compatibility with PDMS.

Under pulsed laser irradiation at 100  $\mu\text{J}$ , the pristine PDMS film exhibited no detectable NLO response (Fig. S47†), confirming that the polymer matrix has negligible influence on the NLO properties. As shown in Fig. 5d and e, the NLO and OPL responses of **Pt-2b@PDMS** increased with **Pt-2b** concentration. The  $T_{\min}$  dropped from 0.46 (0.05 wt%) to 0.11 (1.00 wt%), while the  $\beta_{\text{eff}}$  value increased accordingly, indicating that the NLO performance was concentration-dependent. Table S15† summarizes the linear and NLO parameters of **Pt-2b@PDMS** films at various

concentrations. At 1.00 wt%,  $\beta_{\text{eff}}$  reached  $965.83 \text{ cm GW}^{-1}$ , rivaling or surpassing the  $\beta_{\text{eff}}$  values of the state-of-the-art NLO materials (Table 3).<sup>14,61,62</sup> Besides, **Pt-2b@PDMS-1.00 wt%** demonstrated excellent OPL performance, with an optical limiting onset threshold ( $F_{\text{ON}}$ , defined as the incident fluence at 95% linear transmittance) and  $F_{\text{OL}}$  value of only 0.037 and 0.26  $\text{J cm}^{-2}$ , respectively (Fig. 5f). As illustrated in Fig. 5g and Table 3, its performance surpassed those of many representative solid-state OPL limiters, including TTF-Pt(bzimib),<sup>9</sup> metal clusters ( $\text{V}_9\text{Mo}_1$  and InOC-19),<sup>22,63</sup> Al molecular rings (AlOC-93 and AlOC-135),<sup>53,54</sup> MOF ( $\text{ZnTPy-1}$ ),<sup>14</sup> COF ( $\text{CuPc-PI-COF-1}$ ),<sup>64</sup> and composites ( $(\text{MX@NCS})_4$  and  $\text{MoS}_2\text{-PAN}$ ).<sup>65,66</sup>

Compared with the solution state, **Pt-2b@PDMS** exhibited significantly enhanced OPL performance, with a nearly 5 times higher  $\beta_{\text{eff}}$  value (Fig. S48†). This enhancement can be attributed to the suppressed molecular distortion and reduced  $^3\text{O}_2$ -induced  $T_1$  state quenching in the solid matrix, thereby increasing  $T_1$  state populations. To highlight the advantages of **Pt-2b**, a comparison with **C60@PDMS** showed that **Pt-2b@PDMS** not only displayed a stronger OPL performance but also a higher transparency (Fig. S49 and S50†). These findings



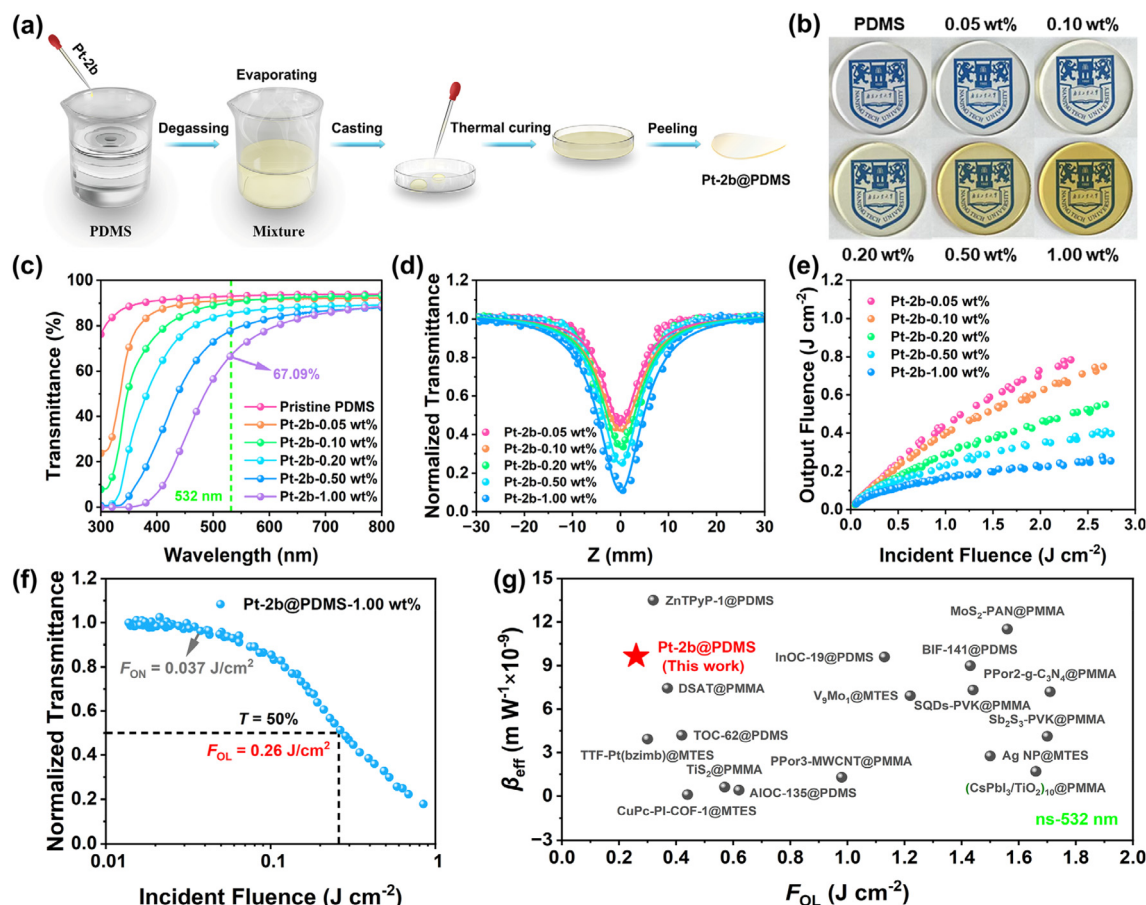


**Fig. 5** (a) Schematic of the preparation process for Pt-2b@PDMS films. (b) Optical photographs of Pt-2b@PDMS films at various concentrations (diameter: 40 mm; thickness: 2 mm). (c) Linear transmittance spectra of Pt-2b@PDMS films. (d) Open-aperture Z-scan curves and (e) output fluence versus input fluence curves for Pt-2b@PDMS films at various concentrations at 532 nm. (f) Nonlinear transmittance versus input fluence curve of Pt-2b@PDMS-1.00 wt%. (g) Comparison of the  $\beta_{\text{eff}}$  and  $F_{\text{OL}}$  values of Pt-2b@PDMS-1.00 wt% with those of representative solid-state optical limiters.

**Table 3** Comparison of the third-order NLO properties of representative solid-state optical limiters at 532 nm

Sample	Parameters <sup>a</sup>	$L^b$ (mm)	$c^c$ (wt %)	$T_0^d$ (%)	$\beta^e$ (cm GW <sup>-1</sup> )	$F_{\text{OL}}^f$ (J cm <sup>-2</sup> )	Ref.
Pt-2b@PDMS	4 ns, 10 Hz	2	1.00	67	965.83	0.26	<b>This work</b>
AlOC-135@PDMS	8.5 ns, 10 Hz	—	—	51	41	0.62	<i>Inorg. Chem. Front.</i> , 2024, <b>11</b> , 462–469 <sup>67</sup>
AlOC-93@PDMS	8.5 ns, 10 Hz	2	—	38	71.80	0.12	<i>Aggregate</i> , 2023, <b>4</b> , e264 <sup>68</sup>
ZnTPyP-1@PDMS	5 ns, 5 Hz	2	0.25	62	1350	0.32	<i>J. Am. Chem. Soc.</i> , 2021, <b>143</b> , 17162–17169 <sup>14</sup>
CuPc-PI-COF-1@MTES	8 ns, 10 Hz	—	—	—	10.72	0.44	<i>Adv. Funct. Mater.</i> , 2024, <b>34</b> , 2404289 <sup>64</sup>
V <sub>3</sub> Mo <sub>4</sub> @MTES	10 ns, 10 Hz	—	1.00	<40	691.79	1.22	<i>Inorg. Chem. Front.</i> , 2022, <b>9</b> , 4413–4424 <sup>63</sup>
TTF-Pt(bzimb)@MTES	8 ns, 10 Hz	—	3.33	41	393	0.30	<i>J. Mater. Chem. C</i> , 2018, <b>6</b> , 8495–8501 <sup>9</sup>
(MX@NCS) <sub>4</sub> /PMMA	6 ns, 1 Hz	1	4.00	—	387	0.21	<i>Small</i> , 2025, 2411146 <sup>65</sup>
DAST@PMMA	6 ns, 2 Hz	0.1	0.125	85	744	0.37	<i>ACS Appl. Mater. Interfaces</i> , 2022, <b>14</b> , 33787–33796 <sup>57</sup>
MoS <sub>2</sub> -PAN@PMMA	8 ns, 2 Hz	—	—	~64	1151.01	1.56	<i>J. Mater. Chem. C</i> , 2017, <b>5</b> , 11920–11926 <sup>66</sup>

<sup>a</sup> Laser pulse width and repetition rate of 532 nm laser. <sup>b</sup> Thickness of the film. <sup>c</sup> Dopant concentration. <sup>d</sup> Linear transmittance at 532 nm. <sup>e</sup> Nonlinear absorption coefficient. <sup>f</sup> Optical limiting threshold.

suggest the potential of Pt-2b@PDMS films for laser protection applications.

### Stability of Pt-2b@PDMS films

Benefiting from its low Young's modulus, Pt-2b@PDMS-1.00 wt% retained its original shape after 100 cycles of stretching, twisting,

and folding (Fig. 6a). The stress–strain curves showed that Pt-2b induced a negligible effect on the mechanical properties of PDMS, with the tensile strength increasing slightly from 8.09 to 8.11 MPa and the modulus from 7.50 to 7.60 MPa (Fig. 6b). TGA analysis revealed that both pristine PDMS and Pt-2b@PDMS-1.00 wt% exhibited  $T_d$  values above 391 °C, confirm-

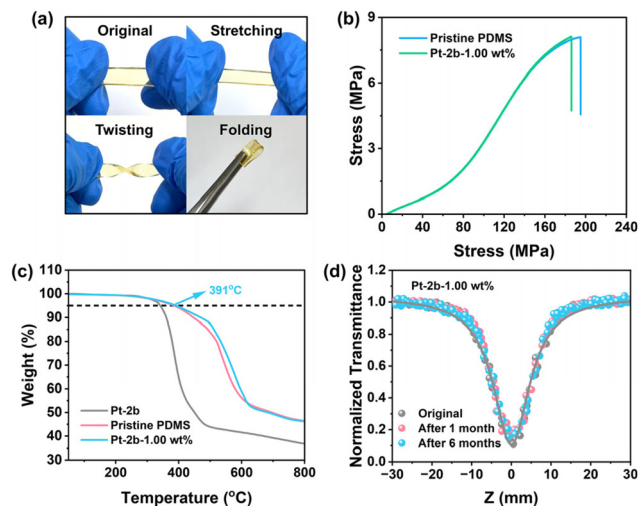


**Fig. 6** (a) Illustration of the mechanical flexibility of Pt-2b@PDMS-1.00 wt%. (b) Stress-strain curves of pristine PDMS and Pt-2b@PDMS-1.00 wt%. (c) TGA curves of Pt-2b, pristine PDMS, and Pt-2b@PDMS-1.00 wt%. (d) Open-aperture Z-scan curves for Pt-2b@PDMS-1.00 wt% after storage for various durations.

ing their excellent thermal stability (Fig. 6c). Moreover, the NLO responses of the film remained nearly unchanged over time, indicating good durability (Fig. 6d). The combination of strong OPL performance, high transparency, and exceptional stability makes Pt-2b@PDMS a promising candidate for OPL devices.

## Conclusions

In summary, six star-shaped Pt(II) complexes were synthesized to tune their photophysical properties and enhance their OPL performance. Spectroscopic and theoretical analyses showed that the  $S_1$  states of Pt-1a–Pt-2c involved mixed  $^1\pi-\pi^*/^1\text{ICT}$  transitions, while the  $T_1$  states were mainly localized  $^3\pi-\pi^*$  transitions on ethynyl ligands. The incorporation of trinuclear Pt centers extended the triplet state lifetimes and enhanced the ESA, with core-ethynyl ligand electronic effects playing crucial roles in regulating the photophysical properties. Pt-2b exhibited outstanding OPL responses while maintaining excellent transparency, surpassing many representative OPL materials. The corresponding Pt-2b@PDMS-1.00 wt% film exhibited a remarkable OPL performance, featuring a high  $\beta_{\text{eff}}$  of  $965.83 \text{ cm GW}^{-1}$  and a low  $F_{\text{OL}}$  of  $0.26 \text{ J cm}^{-2}$ , demonstrating its potential for practical OPL applications. This work highlights the structure–property relationships in Pt(II) complexes and provides a promising strategy for designing next-generation OPL materials. Future work will explore their broadband OPL properties in the NIR region and further investigate their application in flexible photonic devices.

## Author contributions

Lai Hu: methodology, data curation, writing – original draft; Zhiyuan Chen: investigation; Zhi Zhao: data curation; Ruiqi

Chen: conceptualization; Senqiang Zhu: conceptualization, writing – review and editing; Rui Liu: funding acquisition, supervision; Hongjun Zhu: funding acquisition, supervision.

## Conflicts of interest

There are no conflicts to declare.

## Data availability

The data supporting this article have been included as part of the ESI.†

## Acknowledgements

The authors greatly acknowledge the National Key R&D Program of China (2023YFA0913600), the Natural Science Foundation of Jiangsu Province (BK20220351) and the Natural Science Foundation of the Jiangsu Higher Education Institutions of China (No. 22KJB150027) for the financial support.

## References

- Q. Guo, R. Sekine, L. Ledezma, R. Nehra, D. J. Dean, A. Roy, R. M. Gray, S. Jahani and A. Marandi, Femtojoule Femtosecond All-Optical Switching in Lithium Niobate Nanophotonics, *Nat. Photonics*, 2022, **16**, 625–631.
- K. Geng, Y. Sun, Y. Zhao, Z. Shao, Y. Wei, J. Huang, Y. Cui, X. Xu and H. Hou, Giant Enhancement of Optical Nonlinearity by Manipulating Guest Molecular Stacking Modes in Metal–Organic Frameworks, *J. Am. Chem. Soc.*, 2025, **147**, 9844–9857.
- Z. Sun, T. Hasan, F. Torrisi, D. Popa, G. Privitera, F. Wang, F. Bonaccorso, D. M. Basko and A. C. Ferrari, Graphene Mode-Locked Ultrafast Laser, *ACS Nano*, 2010, **4**, 803–810.
- D. Dini, M. J. F. Calvete and M. Hanack, Nonlinear Optical Materials for the Smart Filtering of Optical Radiation, *Chem. Rev.*, 2016, **116**, 13043–13233.
- X. Feng, Z. Shi, J. Chen, T. Yu, X. Jiang, G. Du, J. Qiu and S. Zhou, All-Inorganic Transparent Composite Materials for Optical Limiting, *Adv. Opt. Mater.*, 2020, **8**, 1902143.
- K. S. Krishna, C. S. S. Sandeep, R. Philip and M. Eswaramoorthy, Mixing Does the Magic: A Rapid Synthesis of High Surface Area Noble Metal Nanosponges Showing Broadband Nonlinear Optical Response, *ACS Nano*, 2010, **4**, 2681–2688.
- Y. Song, J. Sun, X. He, M. Liao, J. Zhao, W. Zeng, S. Zhou and H. Chen, N-Doped Nonalternant Nanoribbons with Excellent Nonlinear Optical Performance, *Angew. Chem., Int. Ed.*, 2023, **62**, e202306418.
- M. O. Senge, M. Fazekas, E. G. A. Notaras, W. J. Blau, M. Zawadzka, O. B. Locos and E. M. Ni, Mhuircheartaigh,

- Nonlinear Optical Properties of Porphyrins, *Adv. Mater.*, 2007, **19**, 2737–2774.
- 9 J. Sun, B. Yuan, X. Hou, C. Yan, X. Sun, Z. Xie, X. Shao and S. Zhou, Broadband Optical Limiting of a Novel Twisted Tetrathiafulvalene Incorporated Donor–Acceptor Material and Its Ormosil Gel Glasses, *J. Mater. Chem. C*, 2018, **6**, 8495–8501.
  - 10 Z. Liu, J. Sun, C. Yan, Z. Xie, G. Zhang, X. Shao, D. Zhang and S. Zhou, Diketopyrrolopyrrole Based Donor–Acceptor  $\pi$ -Conjugated Copolymers with near-Infrared Absorption for 532 and 1064 nm Nonlinear Optical Materials, *J. Mater. Chem. C*, 2020, **8**, 12993–13000.
  - 11 S. Hirata, K. Totani, T. Yamashita, C. Adachi and M. Vacha, Large Reverse Saturable Absorption under Weak Continuous Incoherent Light, *Nat. Mater.*, 2014, **13**, 938–946.
  - 12 B. Fang, Y. Zhu, L. Hu, Y. Shen, G. Jiang, Q. Zhang, X. Tian, S. Li, H. Zhou, J. Wu and Y. Tian, Series of C<sup>N</sup>C Cyclometalated Pt(II) Complexes: Synthesis, Crystal Structures, and Nonlinear Optical Properties in the Near-Infrared Region, *Inorg. Chem.*, 2018, **57**, 14134–14143.
  - 13 Z.-Z. Ma, Q.-H. Li, Z. Wang, Z.-G. Gu and J. Zhang, Electrically Regulating Nonlinear Optical Limiting of Metal–Organic Framework Film, *Nat. Commun.*, 2022, **13**, 6347.
  - 14 D.-J. Li, Q. Li, Z.-R. Wang, Z.-Z. Ma, Z.-G. Gu and J. Zhang, Interpenetrated Metal–Porphyrinic Framework for Enhanced Nonlinear Optical Limiting, *J. Am. Chem. Soc.*, 2021, **143**, 17162–17169.
  - 15 D.-J. Li, Q. Li, Z.-G. Gu and J. Zhang, Oriented Assembly of 2D Metal–Pyridylporphyrinic Framework Films for Giant Nonlinear Optical Limiting, *Nano Lett.*, 2021, **21**, 10012–10018.
  - 16 Z.-B. Jin, G. Zhou, Y. Han, Z. Huang, Z.-G. Gu and J. Zhang, Topochemical Polymerization at Diacetylene Metal–Organic Framework Thin Films for Tuning Nonlinear Optics, *J. Am. Chem. Soc.*, 2024, **146**, 25016–25027.
  - 17 Y.-H. Xiao, Z.-G. Gu and J. Zhang, Vapor-Assisted Epitaxial Growth of Porphyrin-Based MOF Thin Film for Nonlinear Optical Limiting, *Sci. China: Chem.*, 2020, **63**, 1059–1065.
  - 18 Z.-K. Wang, M.-H. Du, P. Braunstein and J.-P. Lang, A Cut-to-Link Strategy for Cubane-Based Heterometallic Sulfide Clusters with Giant Third-Order Nonlinear Optical Response, *J. Am. Chem. Soc.*, 2023, **145**, 9982–9987.
  - 19 R. Ho-Wu, S. H. Yau and T. Goodson, Linear and Nonlinear Optical Properties of Monolayer-Protected Gold Nanocluster Films, *ACS Nano*, 2016, **10**, 562–572.
  - 20 Y. Liu, Q. Li, D. Li, X. Zhang, W. Fang and J. Zhang, Designable Al<sub>32</sub>–Oxo Clusters with Hydrotalcite-like Structures: Snapshots of Boundary Hydrolysis and Optical Limiting, *Angew. Chem., Int. Ed.*, 2021, **60**, 4849–4854.
  - 21 J. Sun, X. Tang, Z.-H. Liu, Z. Xie, B. Yan, R. Yin, C. Chaolumen, J. Zhang, W. Fang, J. Wei and H. Shen, Labile Ligands Protected Cu<sub>50</sub> Nanoclusters with Tailorable Optical Limiting Effect, *ACS Mater. Lett.*, 2024, **6**, 281–289.
  - 22 X. Sun, X. Yi, J. Zhang and L. Zhang, Sequential Aggregation of Heterometallic {M<sub>4</sub>X<sub>4</sub>}–Cubanes to Wheel-Shaped In<sub>10</sub> Ni<sub>8</sub>-Oxo Clusters for Optical Limiting Application, *Chem. Mater.*, 2023, **35**, 5845–5853.
  - 23 G.-K. Lim, Z.-L. Chen, J. Clark, R. G. S. Goh, W.-H. Ng, H.-W. Tan, R. H. Friend, P. K. H. Ho and L.-L. Chua, Giant Broadband Nonlinear Optical Absorption Response in Dispersed Graphene Single Sheets, *Nat. Photonics*, 2011, **5**, 554–560.
  - 24 D. Lu, J. Zhang, M. Deng, X. Liu, Z. Liu, K. Yin and H. Li, Impressive Nonlinear Optical Response of  $\pi$ -Conjugated, Photoluminescent Soft Nanoparticles in Polymer Matrix, *Carbon*, 2024, **230**, 119607.
  - 25 B. Wang, B. Ma, K. Wang, H. Zhang, Z. Zhang, T. Song, S. Wang, M. Chen, S. Li, Q. Wang and H. Zhang, Fractal Growth of 2D NbSe<sub>2</sub> for Broadband Nonlinear Optical Limiting, *Adv. Funct. Mater.*, 2024, **34**, 2401490.
  - 26 N. Dong, Y. Li, Y. Feng, S. Zhang, X. Zhang, C. Chang, J. Fan, L. Zhang and J. Wang, Optical Limiting and Theoretical Modelling of Layered Transition Metal Dichalcogenide Nanosheets, *Sci. Rep.*, 2015, **5**, 14646.
  - 27 A. Wang, J. Ye, M. G. Humphrey and C. Zhang, Graphene and Carbon–Nanotube Nanohybrids Covalently Functionalized by Porphyrins and Phthalocyanines for Optoelectronic Properties, *Adv. Mater.*, 2018, **30**, 1705704.
  - 28 R. Liu, J. Hu, S. Zhu, J. Lu and H. Zhu, Synergistically Enhanced Optical Limiting Property of Graphene Oxide Hybrid Materials Functionalized with Pt Complexes, *ACS Appl. Mater. Interfaces*, 2017, **9**, 33029–33040.
  - 29 G.-J. Zhou and W.-Y. Wong, Organometallic Acetylides of PtII, AuI and HgII as New Generation Optical Power Limiting Materials, *Chem. Soc. Rev.*, 2011, **40**, 2541.
  - 30 X. Yang, L. Yue, Y. Yu, B. Liu, J. Dang, Y. Sun, G. Zhou, Z. Wu and W. Wong, Strategically Formulating Aggregation–Induced Emission–Active Phosphorescent Emitters by Restricting the Coordination Skeletal Deformation of Pt(II) Complexes Containing Two Independent Monodentate Ligands, *Adv. Opt. Mater.*, 2020, **8**, 2000079.
  - 31 S. Zhu, J. Hu, S. Zhai, Y. Wang, Z. Xu, R. Liu and H. Zhu, AIPE-Active Pt(II) Complexes with a Tunable Triplet Excited State: Design, Mechanochromism and Application in Anti-Counterfeiting, *Inorg. Chem. Front.*, 2020, **7**, 4677–4686.
  - 32 Y. Cheng, D. Jiang, C. Xiao, M. Li, Y. Lin, C. Zhao, Z. Tang, H. Yin and W. Li, A Platinum Complex–Based Dimerized Electron Acceptor for Efficient Organic Solar Cells, *Adv. Energy Mater.*, 2025, 2404632.
  - 33 Y.-S. Wong, M. Ng, M. C.-L. Yeung and V. W.-W. Yam, Platinum(II)-Based Host–Guest Coordination-Driven Supramolecular Co-Assembly Assisted by Pt...Pt and  $\pi$ - $\pi$  Stacking Interactions: A Dual-Selective Luminescence Sensor for Cations and Anions, *J. Am. Chem. Soc.*, 2021, **143**, 973–982.
  - 34 B. Zhang, Y. Li, R. Liu, T. M. Pritchett, J. E. Haley and W. Sun, Extending the Bandwidth of Reverse Saturable Absorption in Platinum Complexes Using Two-Photon-

- Initiated Excited-State Absorption, *ACS Appl. Mater. Interfaces*, 2013, **5**, 565–572.
- 35 H. Jia, B. Küçüköz, Y. Xing, P. Majumdar, C. Zhang, A. Karatay, G. Yaglioglu, A. Elmali, J. Zhao and M. Hayvali, *Trans-Bis(Alkylphosphine) Platinum(II)-Alkynyl Complexes Showing Broadband Visible Light Absorption and Long-Lived Triplet Excited States*, *J. Mater. Chem. C*, 2014, **2**, 9720–9736.
  - 36 A. Haque, L. Xu, R. A. Al-Balushi, M. K. Al-Suti, R. Ilmi, Z. Guo, M. S. Khan, W.-Y. Wong and P. R. Raithby, Cyclometallated Tridentate Platinum(II) Arylacetylide Complexes: Old Wine in New Bottles, *Chem. Soc. Rev.*, 2019, **48**, 5547–5563.
  - 37 C.-L. Ho, Z.-Q. Yu and W.-Y. Wong, Multifunctional Polymetallaynes: Properties, Functions and Applications, *Chem. Soc. Rev.*, 2016, **45**, 5264–5295.
  - 38 G.-J. Zhou, W.-Y. Wong, C. Ye and Z. Lin, Optical Power Limiters Based on Colorless Di-, Oligo-, and Polymetallaynes: Highly Transparent Materials for Eye Protection Devices, *Adv. Funct. Mater.*, 2007, **17**, 963–975.
  - 39 M. An, X. Yan, Z. Tian, J. Zhao, B. Liu, F. Dang, X. Yang, Y. Wu, G. Zhou, Y. Ren and L. Gao, Optimized Trade-Offs between Triplet Emission and Transparency in Pt(II) Acetylides through Phenylsulfonyl Units for Achieving Good Optical Power Limiting Performance, *J. Mater. Chem. C*, 2016, **4**, 5626–5633.
  - 40 G. G. Dubinina, R. S. Price, K. A. Abboud, G. Wicks, P. Wnuk, Y. Stepanenko, M. Drobizhev, A. Rebane and K. S. Schanze, Phenylene Vinylene Platinum(II) Acetylides with Prodigious Two-Photon Absorption, *J. Am. Chem. Soc.*, 2012, **134**, 19346–19349.
  - 41 G. Zhou, W. Wong, S. Poon, C. Ye and Z. Lin, Symmetric Versus Unsymmetric Platinum(II) Bis(Aryleneethynylene)s with Distinct Electronic Structures for Optical Power Limiting/Optical Transparency Trade-off Optimization, *Adv. Funct. Mater.*, 2009, **19**, 531–544.
  - 42 Z. Cai, M. Zhou, B. Li, Y. Chen, F. Jin and J. Huang, Investigation of Photophysical Properties of New Branched Compounds with Triazine and Benzimidazole Units, *New J. Chem.*, 2014, **38**, 3042.
  - 43 R. L. Roberts, T. Schwich, T. C. Corkery, M. P. Cifuentes, K. A. Green, J. D. Farmer, P. J. Low, T. B. Marder, M. Samoc and M. G. Humphrey, Organometallic Complexes for Nonlinear Optics. 45. Dispersion of the Third-Order Nonlinear Optical Properties of Triphenylamine-Cored Alkynylruthenium Dendrimers, *Adv. Mater.*, 2009, **21**, 2318–2322.
  - 44 X. Yang, B. Jiao, J.-S. Dang, Y. Sun, Y. Wu, G. Zhou and W.-Y. Wong, Achieving High-Performance Solution-Processed Orange OLEDs with the Phosphorescent Cyclometallated Trinuclear Pt(II) Complex, *ACS Appl. Mater. Interfaces*, 2018, **10**, 10227–10235.
  - 45 L. Zhang, M. Morshedi and M. G. Humphrey, Outstanding Multi-Photon Absorption at  $\pi$ -Delocalizable Metallodendrimers, *Angew. Chem., Int. Ed.*, 2022, **61**, e202116181.
  - 46 C. Yao, Z. Tian, D. Jin, F. Zhao, Y. Sun, X. Yang, G. Zhou and W.-Y. Wong, Platinum(II) Acetylide Complexes with Star- and V-Shaped Configurations Possessing Good Trade-off between Optical Transparency and Optical Power Limiting Performance, *J. Mater. Chem. C*, 2017, **5**, 11672–11682.
  - 47 Z. Chen, A. K.-W. Chan, V. C.-H. Wong and V. W.-W. Yam, A Supramolecular Strategy toward an Efficient and Selective Capture of Platinum(II) Complexes, *J. Am. Chem. Soc.*, 2019, **141**, 11204–11211.
  - 48 Y.-F. Zhong, H. Zhang, G. Mu, W.-T. Liu, Q. Cao, C.-P. Tan, L.-N. Ji and Z.-W. Mao, Nucleus-Localized Platinum(II)-Triphenylamine Complexes as Potent Photodynamic Anticancer Agents, *Inorg. Chem. Front.*, 2019, **6**, 2817–2823.
  - 49 T. Yasuda, T. Shimizu, F. Liu, G. Ungar and T. Kato, Electro-Functional Octupolar  $\pi$ -Conjugated Columnar Liquid Crystals, *J. Am. Chem. Soc.*, 2011, **133**, 13437–13444.
  - 50 W. Yang, A. Karatay, J. Zhao, J. Song, L. Zhao, Y. Xing, C. Zhang, C. He, H. G. Yaglioglu, M. Hayvali, A. Elmali and B. Küçüköz, Near-IR Broadband-Absorbing *Trans*-Bisphosphine Pt(II) Bisacetylide Complexes: Preparation and Study of the Photophysics, *Inorg. Chem.*, 2015, **54**, 7492–7505.
  - 51 J. Lu, Q. Pan, S. Zhu, R. Liu and H. Zhu, Ligand-Mediated Photophysics Adjustability in Bis-Tridentate Ir(III) Complexes and Their Application in Efficient Optical Limiting Materials, *Inorg. Chem.*, 2021, **60**, 12835–12846.
  - 52 J. M. Keller, K. D. Glusac, E. O. Danilov, S. McIlroy, P. Sreearuthai, A. R. Cook, H. Jiang, J. R. Miller and K. S. Schanze, Negative Polaron and Triplet Exciton Diffusion in Organometallic “Molecular Wires”, *J. Am. Chem. Soc.*, 2011, **133**, 11289–11298.
  - 53 W. He, M. Y. Livshits, D. A. Dickie, Z. Zhang, L. E. Mejiaortega, J. J. Rack, Q. Wu and Y. Qin, “Roller-Wheel”-Type Pt-Containing Small Molecules and the Impact of “Rollers” on Material Crystallinity, Electronic Properties, and Solar Cell Performance, *J. Am. Chem. Soc.*, 2017, **139**, 14109–14119.
  - 54 Z. Yin, X. Chang, J. Zang, S. Lin, Z. Zhou, T. Liu, L. Ding, H. Peng and Y. Fang, A Triphenylamine-Based Pt(II) Metallacage via Coordination-Driven Self-Assembly for Nonlinear Optical Power Limiting, *J. Mater. Chem. C*, 2022, **10**, 10429–10438.
  - 55 Y. Du, N. Dong, M. Zhang, B. Jiang, N. Sun, Y. Luo, S. Zhang, G. Wang and J. Wang, Poly(Arylene Ether)s Based on Platinum(II) Acetylide Complexes: Synthesis and Photophysical and Nonlinear Absorption Properties, *J. Mater. Chem. C*, 2018, **6**, 7317–7325.
  - 56 J. Wang, J. Zhao, S. Han, Y. Li, W. Zeng, J. Sun and S. Zhou, Significant Enhancement of Reverse Saturable Absorption Ability via Pt(II) Incorporation into the Conjugated Backbone of Benzo[1,2-b :4,5-b']Dithiophene-Based Donor-Acceptor Copolymers, *Macromolecules*, 2024, **57**, 1030–1037.
  - 57 M. Zhang, X. Xu, J. Liu, Y. Jiang, J. Wang, N. Dong, C. Chen, B. Zhu, Y. Liang, T. Fan and J. Xu, All-Organic



- Composite Films for High Flexibility and Giant Nonlinear Optical Limiting Responses, *ACS Appl. Mater. Interfaces*, 2022, **14**, 33787–33796.
- 58 F. Xing, J. Wang, Z. Wang, Y. Li, X. Gou, H. Zhang, S. Zhou, J. Zhao and Z. Xie, Covalently Silane-Functionalized Antimonene Nanosheets and Their Copolymerized Gel Glasses for Broadband Vis–NIR Optical Limiting, *ACS Appl. Mater. Interfaces*, 2021, **13**, 897–903.
- 59 W. Feng, K. Liu, J. Zang, G. Wang, R. Miao, L. Ding, T. Liu, J. Kong and Y. Fang, Flexible and Transparent Oligothiophene-o-Carborane-Containing Hybrid Films for Nonlinear Optical Limiting Based on Efficient Two-Photon Absorption, *ACS Appl. Mater. Interfaces*, 2021, **13**, 28985–28995.
- 60 Z. Xie, F. Wang and C. Liu, Organic–Inorganic Hybrid Functional Carbon Dot Gel Glasses, *Adv. Mater.*, 2012, **24**, 1716–1721.
- 61 A. A. Noble, I. H. Joe and S. Nazar, Defect-Controlled Fabrication of Reduced Graphene Oxide/ZnO/PMMA-Based Solid-State Optical Limiting Filters with SA/RSA Switching Property, *Carbon*, 2024, **228**, 119435.
- 62 J.-W. Li, W. Dong, Y. Liu, Y. Li, L.-Y. Qiao, G.-L. Liu, H. Zhang, C. Wang, H.-L. Zheng and J.-Q. Zhao, Water-Stable Zero-Dimensional Hybrid Zinc Halide Modulated by  $\pi$ – $\pi$  Interactions: Efficient Blue Light Emission and Third-Order Nonlinear Optical Response, *Inorg. Chem. Front.*, 2024, **11**, 8431–8438.
- 63 L.-S. Wang, Y. Wang, C.-L. Lv, C. Guo, F.-Y. Xing, Y.-J. Dong, Z. Xie, S.-Y. Zhou and Y.-G. Wei, Polyoxometalates with Tunable Third-Order Nonlinear Optical and Superbroadband Optical Limiting Properties, *Inorg. Chem. Front.*, 2022, **9**, 4413–4424.
- 64 B. Han, B. Liang, E. Zhang, J. Li, Y. Li, Q. Zhang, Z. Xie, H. Wang and J. Jiang, Phthalocyanine Covalent Organic Frameworks: Dimensionality Effect on Third-Order Nonlinear Optical Properties, *Adv. Funct. Mater.*, 2024, **34**, 2404289.
- 65 J. Wei, F. Hu, C. Lv, L. Bian, X. Quan and Q. Ouyang, Fabrication of Dual-Functional MXene@NiCo<sub>2</sub>S<sub>4</sub> Composites with Enhanced Nonlinear Optical and Electrochemical Properties, *Small*, 2025, **21**, 2411146.
- 66 M. Shi, N. Dong, N. He, Y. Wan, H. Cheng, M. Han, J. Wang and Y. Chen, MoS<sub>2</sub> Nanosheets Covalently Functionalized with Polyacrylonitrile: Synthesis and Broadband Laser Protection Performance, *J. Mater. Chem. C*, 2017, **5**, 11920–11926.
- 67 S.-T. Wang, X. Qi, R.-Q. Chen, W.-H. Fang and J. Zhang, Two Solvent-Dependent Al<sub>16</sub> Nanorings: Design, Synthesis and Nonlinear Optical Limiting Behavior, *Inorg. Chem. Front.*, 2024, **11**, 462–469.
- 68 S. Wang, Y. Liu, C. Feng, W. Fang and J. Zhang, The Largest Aluminum Molecular Rings: Phenol-thermal Synthesis, Photoluminescence, and Optical Limiting, *Aggregate*, 2023, **4**, e264.